ABSTRACT

Title of thesis: RADIATION DOSE REDUCTION STRATEGIES FOR INTRAOPERATIVE GUIDANCE AND NAVIGATION USING CT

Avanti Shetye, Master of Science, 2007.

Thesis directed by: Dr. Raj Shekhar
Department of Electrical and Computer Engineering

The advent of 64-slice computed tomography (CT) with high-speed scanning makes CT a highly attractive and powerful tool for navigating image-guided procedures. Interactive navigation needs scanning to be performed over extended time periods or even continuously. However, continuous CT is likely to expose the patient and the physician to potentially unsafe radiation levels. Before CT can be used appropriately for navigational purposes, the dose problem must be solved. Simple dose reduction is not adequate, because it degrades image quality. This study proposes two strategies for dose reduction; the first is the use of a statistical approach representing the stochastic nature of noisy projection data at low doses to lessen image degradation and the second, the modeling of local image deformations in a continuous scan. Taking advantage of modern CT scanners and specialized hardware, it may be possible to perform continuous CT scanning at acceptable radiation doses for intraoperative navigation.

RADIATION DOSE REDUCTION STRATEGIES FOR INTRAOPERATIVE GUIDANCE AND NAVIGATION USING CT

By

Avanti Satish Shetye

Thesis submitted to the Faculty of the Graduate School of the
University of Maryland, College Park in partial fulfillment
of the requirements for the degree of
Master of Science
2007

Advisory committee:
Professor Raj Shekhar, Chair
Professor Rama Chellappa
Professor Jonathan Simon

Dedication

“To my dearest Aai and Pappa, and to the loving memory of my brother Yogendra...”

Acknowledgements

I extend my sincere appreciation toward my advisor, Dr. Raj Shekhar for giving me the wonderful opportunity of working in the field of medical imaging. Through his patient guidance, encouragement and innovative ideas, he created a dynamic environment in the lab that challenged me to accomplish my research pursuits and developed in me a deep respect for innovation. My interaction with him has made me confident to face challenges in my professional career with a positive attitude. Thank you Dr. Shekhar for all that you have done for me!!

I thank Prof. Rama Chellappa and Dr. Jonathan Simon for agreeing to serve on my thesis committee and for sparing their invaluable time reviewing my manuscript. Special thanks to Prof. Andre Tits at the University of Maryland, Prof. Kenneth Lange at the UCLA and Dr. Jeffrey Fessler at the University of Michigan for their prompt responses to my research queries.

I express my heartfelt gratitude toward Bulent Bayraktar, Adam Covitch and Abraham Cohn at Philips Medical Systems, Ohio and Pavan at the University of Maryland for their assistance in providing experimental data for this project. I thank my lab-members Will, Jianzhou, Vivek, Yash and Peng for sharing their thoughts and ideas on technical matters.

On a personal note, I would like to thank my beautiful friends Rupali, Om, Pankaj, Arun, Nirmala and several others for being a wonderful support system during my days of distress. I would like to acknowledge the love and support of my sweetheart Tushar, who

courageously endured all my eccentricities. Finally, I would like to acknowledge the love and blessings of my family over all these years: my parents Sudha and Satish Shetye, my late brother Yogendra, my aunts Smita Maushi and Pushpa Maushi, and my late grandparents, Bai Aaji, Baba Ajoba and Atya Aaji.

Table of contents

List of Figures

CHAPTER 1

Introduction and motivation

The method of choice for many surgical procedures has shifted from traditional open surgery to the use of less invasive means, a transition facilitated by the introduction of minimally invasive techniques more than a decade ago. Such procedures are often performed through 3 or 4 small skin ports (keyhole-size holes) instead of the 6- to 8-inch incisions required for traditional surgery [1]. The results are reduced trauma to the body, shorter recovery times and lower costs. However, the utility of such procedures is limited without a clear representation of the anatomy undergoing the procedure. The ability of the clinician will be greatly enhanced if three-dimensional (3D) visualization of this anatomy is available to guide such procedures [2].

Computed tomography (CT), a widely used diagnostic technique, is known to provide a highly accurate volumetric representation of the anatomy, with good contrast resolution. A CT scanner can create instantaneous 3D representations of the internal anatomy with good contrast resolution. This gives CT an edge over other imaging modalities in terms of continuous visualization of and navigation through structures. Some minimally invasive procedures utilize this benefit by acquiring a preoperative CT scan for guidance. This approach is limited, because it does not provide updated information on intraoperative anatomic deformations and deformations since the time of preoperative CT. A continuous CT-guided approach can represent intraoperative anatomy accurately, but such scanning is practical only if radiation is reduced to a minimal level with a high image reconstruction speed. Commercially available CT scanners employ a filtered

backprojection (FBP) technique for image reconstruction. Although useful in many imaging applications, the FBP technique does not allow dose reduction without significantly degrading image quality. Continuous CT with FBP reconstruction, then, would expose both patient and practitioner to elevated levels of radiation. FBP also causes streak artifacts when metal is in the field of view, for example during surgery.

The motivation behind this study is to utilize the benefit of 3D visualization achieved through CT, but at a greatly reduced radiation dose without compromising image quality. Iterative techniques using maximum likelihood are proven to replicate Poisson statistics for positron emission tomography, single-photon emission computed tomography and CT [3]-[8]. Although statistical reconstruction is computationally expensive, the suboptimal FBP approach is certainly not an acceptable one for reconstructing noisy projection data. This study suggests two dose reduction strategies for developing a minimally invasive surgical system under a continuous CT guidance and elimination of metal artifacts resulting from surgical tools with the use of tracking tools. Our first strategy is the achievability of dose reduction through replacement of FBP with a statistical approach using maximum likelihood expectation maximization (MLEM) for image reconstruction. Our second strategy is the achievability of dose reduction for continuous CT through reduction in the number of projections using gradient descent optimization to iteratively model the local intraoperative anatomic deformations.

The reconstruction process is described in chapter 2 striking distinctions between two widely used approaches to CT reconstruction. The theory behind our dose reduction

strategies is outlined in chapter 3 followed by the results in chapter 4. Inferences from this study and some practical issues are discussed in chapter 5. Another novel method for dose reduction that combines the two strategies is currently under investigation and is presented in chapter 6.

CHAPTER 2

The reconstruction process

Inside a typical 3rd generation (3G) CT scanner is a gantry that has an x-ray tube on one side and arc-shaped array of detectors mounted on the opposite side. The x-ray photons emitted by the tube are captured by the detectors after being attenuated through the object under consideration to generate projection data. Image reconstruction is the process of determining the attenuation coefficients at all locations in the cross-section of the object using available projection data. Several such closely spaced cross-sections are stacked together to generate a volumetric representation of the object. CT is frequently used for diagnostic purposes. A pictorial representation of a typical 3G CT scan is demonstrated in Figure 1.

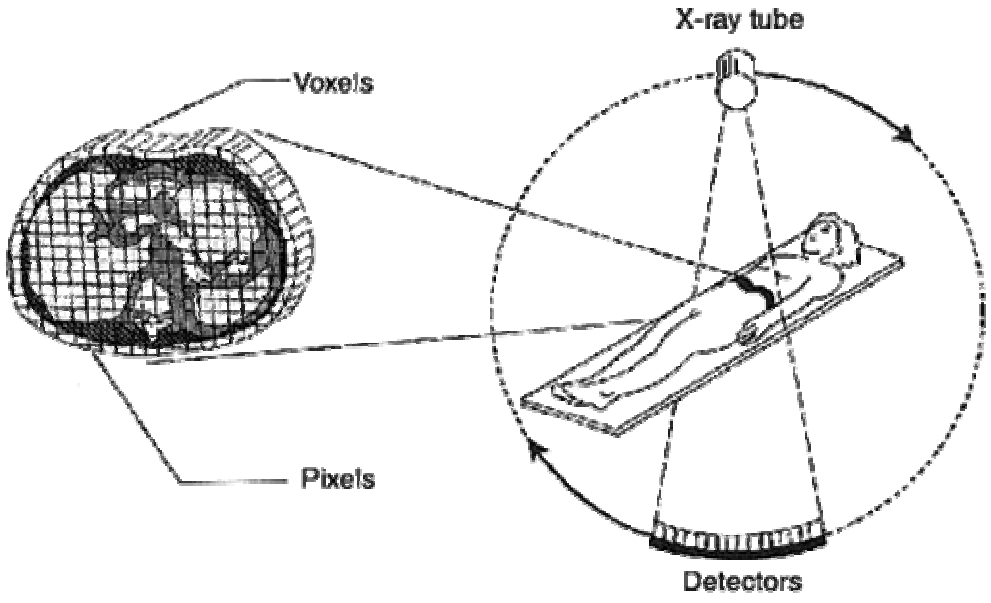

Figure 1: The geometry of a typical 3GCT scan: the x-ray tube and detectors rotate, with the axis of rotation running from the patient's head to toe [9].

A typical 4th generation (4G) scanner consisting of a stationary ring of detectors with a rotating x-ray source is shown in Figure 2 [10].

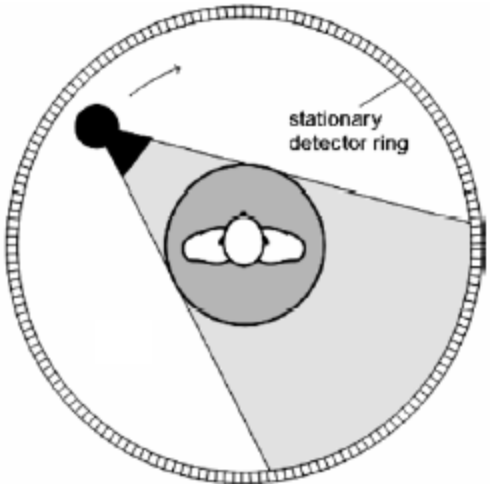

Figure 2: Schematic of a 4G CT scanner.

2.1. Conventional approach to CT reconstruction

FBP, the conventional approach to CT reconstruction, uses the Fourier slice theorem to arrive at a closed-form deterministic solution to finding attenuation coefficients. The underlying assumption behind this theorem is that each projection represents an independent measurement of the object. The details can be found in [11]. The advantage of FBP is that the process of reconstruction can be started as soon as the first projection has been measured, speeding up the process and reducing the requirements for storage. FBP reconstruction produces high-quality images at high radiation doses. However, the image quality begins to deteriorate as the x-ray dose is reduced. Dose reduction is a crucial requirement for the application of CT in interventional purposes, where patients and practitioners will be exposed to continuous radiation over the duration of surgery.

2.2. Statistical approach to CT reconstruction

The process of photon generation in an x-ray tube can be approximated using the Poisson distribution. Iterative techniques such as MLEM capture the stochastic variations in photon counts accurately (unlike the deterministic FBP approach) yielding more accurate reconstructions at much lower radiation doses. Maximum likelihood has been shown to have excellent theoretical properties that model the statistical nature of CT in a realistic manner [7]. The objective of this algorithm is to maximize the complete likelihood of the photons entering each pixel along the projection ray, given the number of photons detected by the detector at the projection, parameterized by the current estimate of pixel intensities. The new estimate of the pixel intensity can be approximated to a closed-form solution. The original MLEM algorithm is presented in brief in the next chapter. For a detailed description of the original algorithm, the interested reader is referred to [7].

CHAPTER 3

Dose reduction

3.1. MLEM Algorithm

Our algorithm has been developed based on the Lange & Carson [7] framework. The concept is described for parallel beam geometry and can be extended easily to the fan beam case. The MLEM algorithm is part of our first dose reduction strategy.

The number of photons detected by scanning air provides a fair approximation to the number of photons generated by the x-ray source. If W_i is the number of photons leaving the source, all W_i photons will be detected in the absence of an attenuating object. Then, in the presence of an attenuating object, if Y_i is the number of photons detected, by Beer's law, each photon leaving the source has an equal probability of reaching the detector. This probability is expressed as:

$$p_i = e^{-\sum_{j \in J_i} l_{ij} \mu_j}, \qquad (1)$$

where l_{ij} is the length of intersection of the i[th] ray with the j[th] pixel, μ_j is the intensity (i.e., attenuation coefficient) of the j[th] pixel and J_i is the set of all pixels traversed by the i[th] ray.

Because Y_i follows a Poisson distribution, the entire log likelihood can be reduced to

$$\ln g(Y, \mu) = \sum_i \left\{ -W_i e^{-\sum_{j \in J_i} l_{ij} \mu_j} - Y_i \sum_{j \in J_i} l_{ij} \mu_j + Y_i \ln W_i - \ln Y_i! \right\}. \qquad (2)$$

The strict concavity, which suggests the existence of a maximum of this likelihood, can be established by the non-negative definiteness of the matrix with elements

$$a_{ik} = \begin{cases} l_{ik} \text{.....} k \in J_i \\ 0 \text{.....} k \notin J_i \end{cases}. \tag{3}$$

In the MLEM algorithm, a reconstruction grid of uniform intensity is used as the initial estimate. Iterating on the reconstruction grid, the log likelihood is maximized and the maximizing image estimate is used as an initial estimate for the next iteration. The closed form solution at the $(n+1)^{th}$ iteration is expressed as:

$$\mu_k^{n+1} = \frac{\sum_{i \in J_i} \left(M_{ik} - N_{ik} \right)}{\frac{1}{2} \sum_{i \in J} \left(M_{ik} + N_{ik} \right) l_{ik}}, \tag{4}$$

where M_{ik} and N_{ik} are the expected number of photons entering and leaving pixel k and are determined using Beer's law (Eq. 1).

3.2. Local deformations

In the context of minimally invasive surgery, if the anatomy were stationary, a preoperative scan would suffice. However, the anatomy is subject to change due to intervention and involuntary motion. Continuous (near real-time) guidance and navigation would require a CT scanner to be operated continually at very high frame acquisition rate. If the frame rate is significantly high, the imaged anatomy will have undergone only a slight redistribution of pixel intensities between successive frames. Starting with the final reconstructed image of the previous time-frame, a good estimate at

the current time-frame can be obtained by modeling the deformations between the current and the previous time-frames using available projection data for the current time-frame.

A free form deformation (FFD) model of [12] using B-splines is used to model the local motion between successive time-frames. The underlying idea of FFDs is to deform an object by modifying the translation vectors of a coarse mesh of control points throughout the object. The resulting deformation when interpolated over the fine mesh of pixels yields a smooth and continuous deformation. B-splines provide a local control over deformation unlike thin-plate splines. The resulting FFD can be written as

$$T(x,y)=\sum_{0}^{3}\sum_{0}^{3}B_l(u)B_m(v)\phi_{i+l,j+m}\,, \tag{5}$$

where the image space is defined by a set $\Omega=\{(x,y)\mid 0\le x<X,0\le y<Y\}$, Φ denotes a mesh of $n_x\times n_y$ control points $\phi_{i,j}$ separated by a uniform spacing δ, $i=\lfloor x/n_x\rfloor-1$, $j=\lfloor y/n_y\rfloor-1$, $u=x/n_x-\lfloor x/n_x\rfloor$ and $v=y/n_y-\lfloor y/n_y\rfloor$ and B_l represents the l^{th} basis function of the B-spline

$$\begin{aligned}B_o(u)&=(1-u)^3/6\\ B_1(u)&=(3u^3-6u^2+4)/6\\ B_2(u)&=(-3u^3+3u^2+3u+1)/6\\ B_3(u)&=u^3/6\end{aligned}. \tag{6}$$

A large spacing of control points enables modeling of global non-rigid deformations and a small spacing of control points enables modeling of local non-rigid deformations.

3.3. Gradient descent optimization

In a gradient descent minimization algorithm, steps are taken iteratively in the current direction of the negative gradient of the cost function $f(\overline{\Phi}_t)$.

$$\overline{\Phi}_{t+1} = \overline{\Phi}_t - \alpha \nabla_{\overline{\Phi}_t} f(\overline{\Phi}_t), \tag{7}$$

where α is a positive step-size parameter, $\overline{\Phi}_t$ is a set of translations of the mesh of control points $\left(\phi_{1,1}, \phi_{1,2}, ..., \phi_{n_x,n_y}\right)^T$ in the x- and y-direction at the t^{th} iteration, gradient $\nabla_{\overline{\Phi}_t} f(\overline{\Phi}_t)$ denotes a vector of partial derivatives $\left(\frac{\partial f(\overline{\Phi}_t)}{\partial \phi_{1,1}}, \frac{\partial f(\overline{\Phi}_t)}{\partial \phi_{1,2}}, ..., \frac{\partial f(\overline{\Phi}_t)}{\partial \phi_{n_x,n_y}}\right)^T$ and $(.)^T$ denotes transpose.

A Radon transform is always unique when sufficient samples of it are available. In two dimensions, if a sufficient set of Radon transform samples is known, then the Radon transform is adequately specified and the cross-section function comprising the pixel intensities can be determined by inverting the Radon transform [13]. Hence the cost function chosen for optimization is the sum of squared differences between scanner-projection data of the deformed image and the Radon transform of the image estimate. (Note that the projection data is the radon transform of the actual deformed image).

A good initial estimate of the image is provided by the final reconstructed image from the previous time-frame. The initial deformation vector $\overline{\Phi}_t$ for the coarse mesh of control points is set to $\overline{0}$. The vector $\overline{\Phi}_t$ is updated using Eq. 7 in the current direction of the negative gradient of the cost function, thus improving its estimate iteratively. A smooth

continuous deformation is obtained from the vector $\overline{\Phi}_t$ through B-spline interpolation (Eq. 5 and 6). The image, used in the calculation of the cost function, is updated through bilinear interpolation of the previous image estimate using the current deformation vector.

The step-size, α, is varied iteratively to avoid convergence to a local optimum solution. A good starting estimate for the step-size was empirically found to be 0.01. If the current value of cost function is better (less) than the previous value, the image is updated and step-size is increased by a factor of 10 for the next iteration. A small step-size leads to a slower convergence. So, to accelerate convergence, the step-size is adaptively changed depending on how well the current step-size performs. If the current value of cost function is worse than the previous one, the step size is reduced by half until a better estimate is obtained. The process is repeated until the terminating condition occurs. A terminating condition is said to have reached if the cost function changes by less than 0.5 for 5 successive iterations, or if the number of iterations exceeds 200, whichever occurs first. To ensure convergence to global minimum, annealing techniques need to be investigated.

CHAPTER 4

Results

The reconstruction algorithms were applied to simulated data from the digital Shepp-Logan phantom and to real projection data from an abdominal phantom representing real anatomy. The reconstruction quality was assessed using power signal-to-noise ratio (PSNR) calculated as:

$$PSNR = 10\log_{10}\frac{(2^{bitdepth}-1)^2}{MSE(A,B)}, \text{ and} \tag{8}$$

$$MSE(A,B) = \frac{\sum_{i=1}^{M}\sum_{j=1}^{N}\left(A_{ij}-B_{ij}\right)^2}{MN}, \tag{9}$$

Where M x N represents the number of pixels in image A and B, A_{ij} represents the intensity of $(i,j)^{th}$ pixel of A and B_{ij} represents the intensity of $(i,j)^{th}$ pixel of B.

4.1. MLEM reconstruction of Shepp-Logan phantom

A 512 x 512 digital Shepp-Logan phantom was generated in MATLAB and projection data was simulated using Beer's law (Eq. 1). Expectation of noise in low-dose sinograms was estimated by fitting a Poisson distribution to the difference between sinograms of images obtained from the low-dose simulator at 200 mAs and at lower doses. This Poisson noise was scaled to the dynamic range of phantom and added to the simulated projections for the digital phantom to generate noisy data resembling low-dose (low tube current) projections, with the assumption that sinogram noise follows Poisson distribution. Reconstructions using the MLEM algorithm yielded better results in terms of

the PSNR values with the original phantom as the reference image than did corresponding reconstructions using FBP.

The digital phantom used in our study is shown in Figure 3. Reconstructions at 11mAs using FBP and MLEM are shown in Figure 4(a) for a visual comparison. To test the reproducibility of our results, reconstructions at 15mAs using the same 2 methods are shown in Figure 4(b). At each of these doses, MLEM led to higher contrast resolution, mimicking that of the original image. PSNRs for these two algorithms at a range of dose levels are summarized in Table 1. A quantitative comparison of the reconstruction qualities achieved through FBP and MLEM is delineated by means of a plot in Figure 5. The comparison shows that MLEM outperforms FBP at any given dose level. Note that a tube current setting of 11mAs is the lowest achievable dose on a Siemens dose simulator. [Courtesy: Baltimore Veteran Affairs Medical Center, MD]

4.2. MLEM reconstruction of abdominal phantom

An abdominal phantom was scanned using a Philips Brilliance 40-slice CT scanner at 120 kV and tube current varying at random from 25 to 250 mAs at the following scanner-console settings. Axial scanning was done at 2-sec cycle time with standard resolution, 16 x 2.5 mm collimation and slice thickness of 5 mm. The number of samples per view was 672 with 1160 views evenly spanned on a circular orbit of 360^{o}. Raw un-preprocessed fan beam data were extracted using scanner software and altered to parallel beam data. The PSNR values suggest that the image quality of MLEM reconstruction degrades less precipitously than that of FBP as the dose level is reduced from 250 to 25

mAs. Figure 6 and Figure 7 provide visual assessments of FBP and MLEM reconstructions. A quantitative assessment is detailed in Table 2 and shown in Figure 8.

Figure 3: A 512 x 512 digital Shepp-Logan phantom.

Table 1:

PSNR comparison between FBP and MLEM for the Shepp-Logan phantom

Dose (mAs)	PSNR for FBP (dB)	PSNR for MLEM (dB)
11	30.08	36.98
15	31.18	37.67
20	32.73	38.56
25	33.09	38.83
30	33.97	39.50
40	34.88	39.96
50	35.86	40.13
70	37.00	40.67
85	37.26	40.90
100	37.36	40.99
150	38.56	41.07

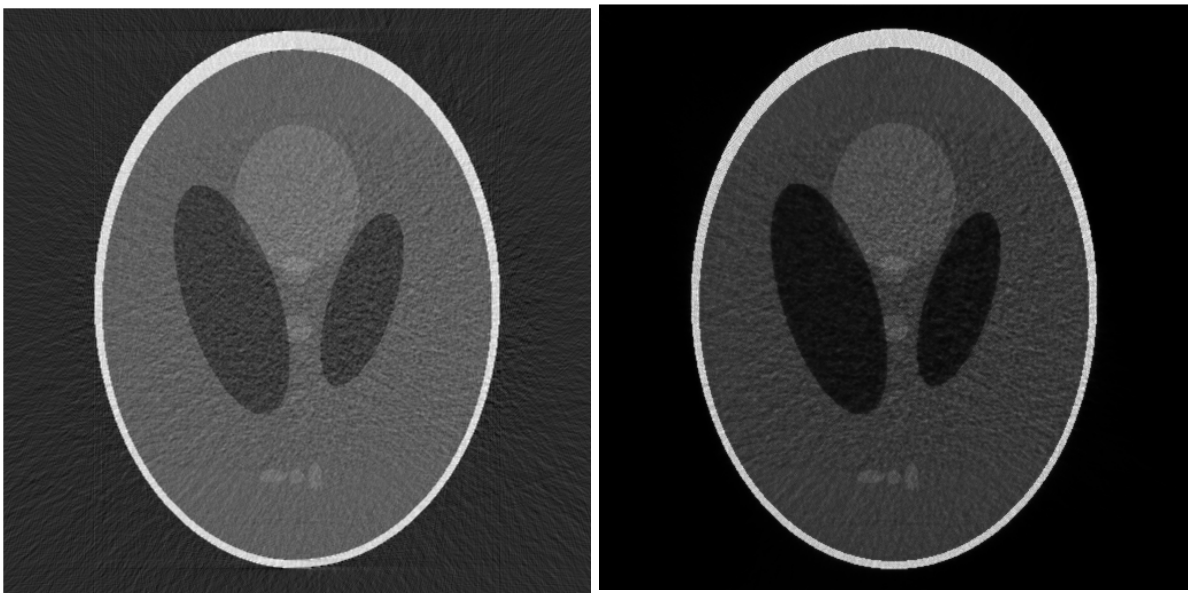

(a) FBP reconstruction at 11 mAs (left) MLEM reconstruction at 11 mAs(right).

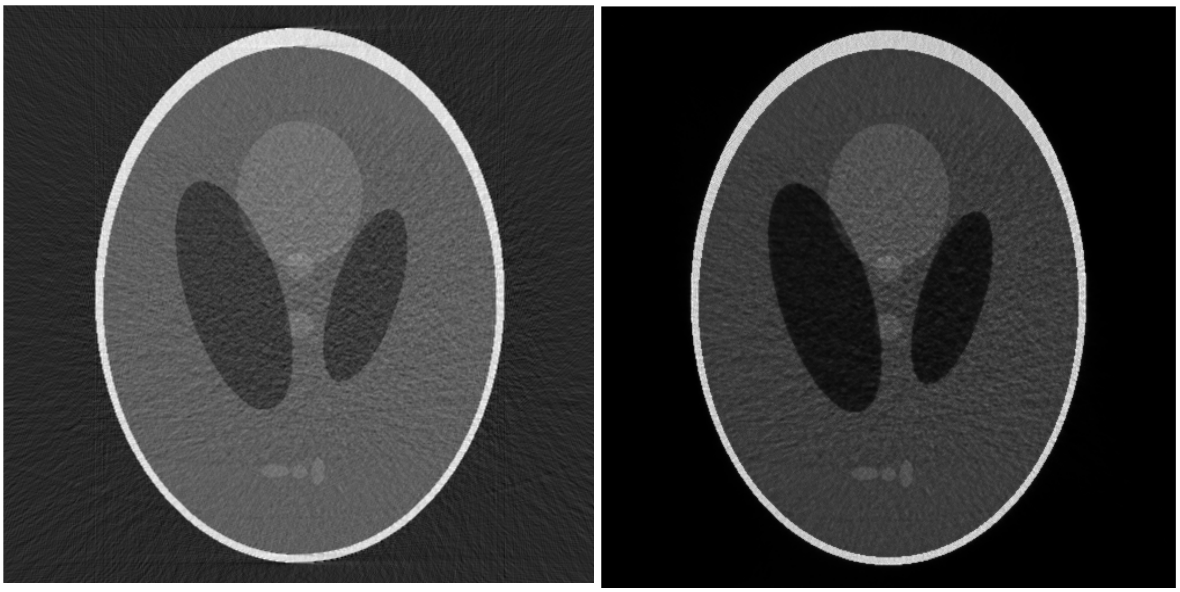

(b) FBP reconstruction at 15 mAs (left) MLEM reconstruction at 15 mAs (right).
Figure 4: Visual comparison of reconstruction quality.

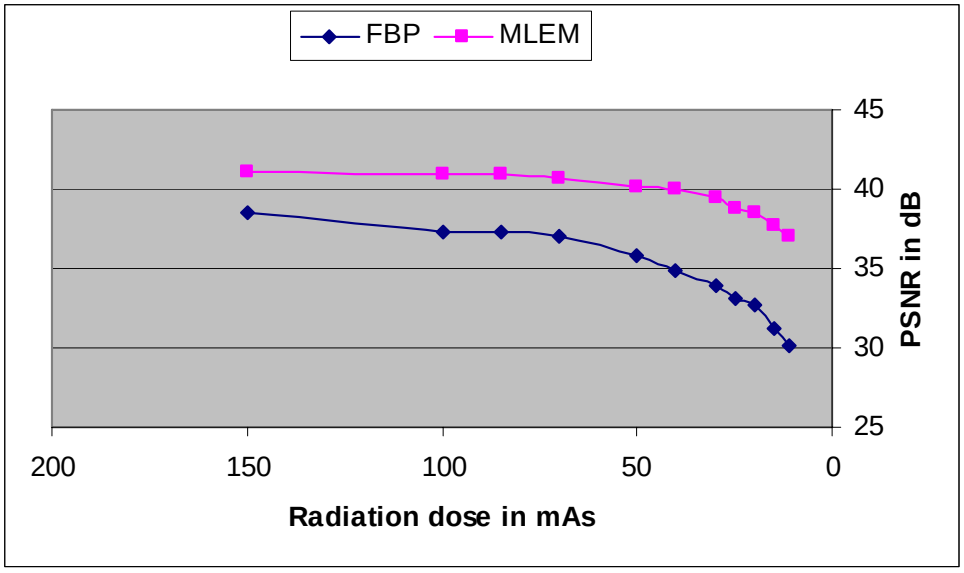

Figure 5: PSNR comparison between FBP and MLEM.

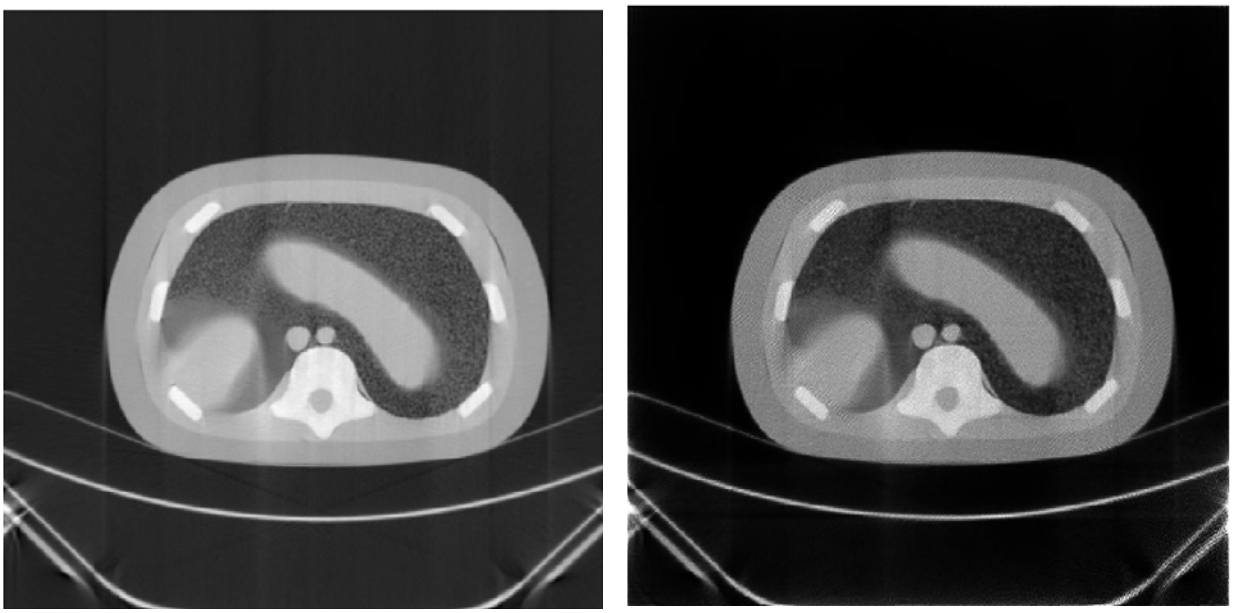

Figure 6: FBP reconstruction (left) and MLEM reconstruction (right) of abdominal phantom at 200 mAs.

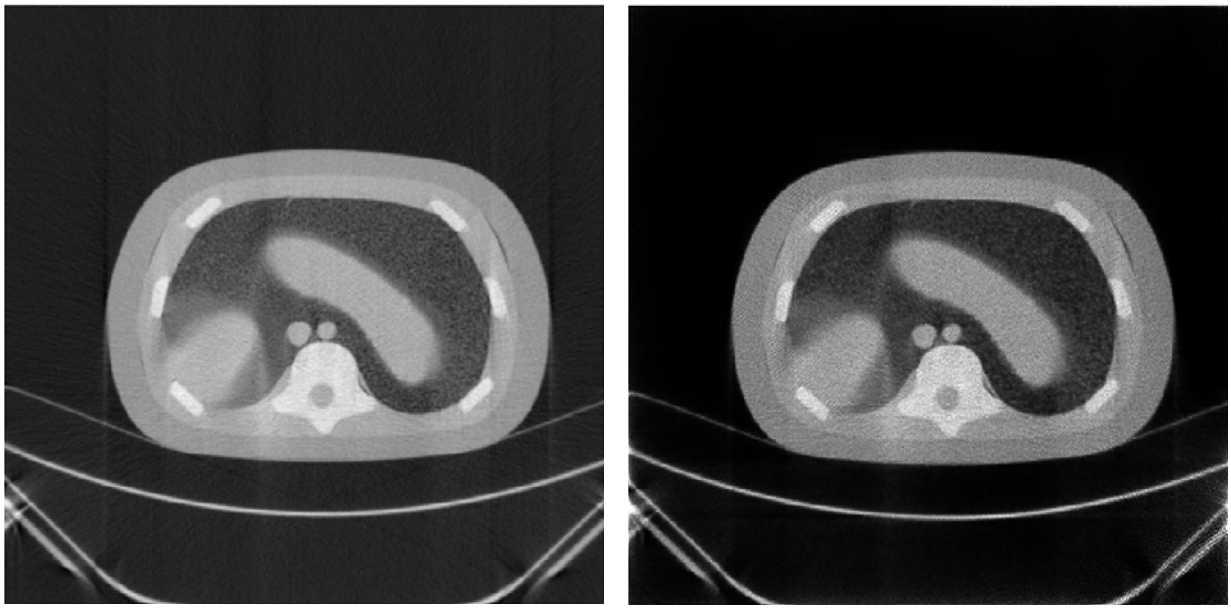

Figure 7: FBP reconstruction (left) and MLEM reconstruction (right) of abdominal phantom at 25 mAs.

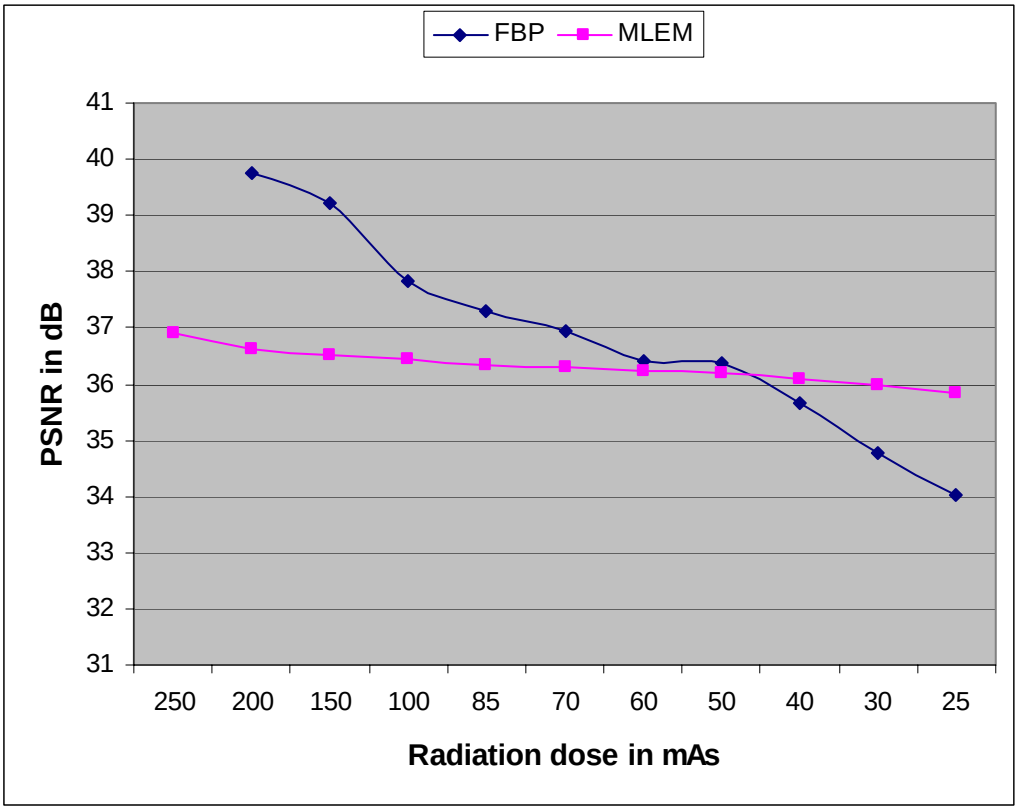

Figure 8: PSNR comparison between FBP and MLEM for abdominal phantom.

Table 2:
PSNR comparison between FBP and MLEM for abdominal phantom

Dose (mAs)	PSNR for FBP (dB)	PSNR for MLEM (dB)
250	36.90	Inf
200	36.63	39.75
150	36.51	39.20
100	36.46	37.85
85	36.34	37.31
70	36.30	36.93
60	36.23	36.40
50	36.19	36.37
40	36.08	35.65
30	35.97	34.79
25	35.85	34.02

4.3. Metal artifact reduction

To demonstrate metal artifact reduction, a high-attenuation object was introduced in a 512 x 512 digital Shepp-Logan phantom at pixel location (190, 295) shown in Figure 9.

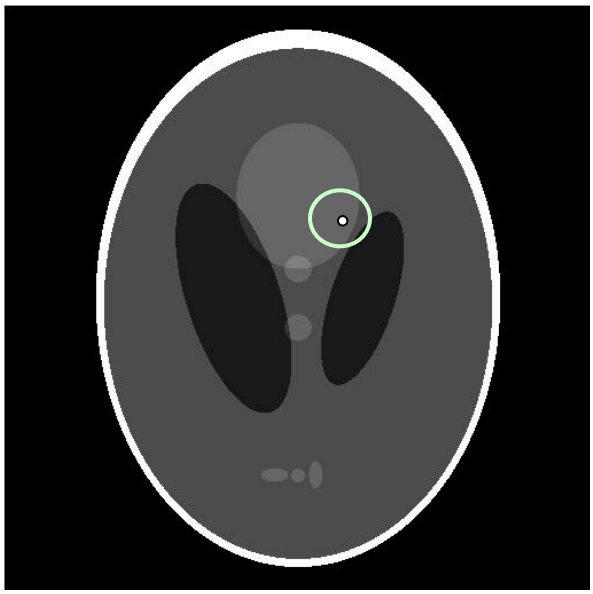

Figure 9: Digital Shepp-Logan phantom with high attenuation pixel at location (190,295). (highlighted for clarity).

The projection data simulated using Beer's law (Eq. 1) was reconstructed using the MLEM algorithm, depicted in Figure 11 (b). With the prior knowledge of the location of

the high-attenuation object, the MLEM algorithm was able to accurately eliminate the FBP algorithm-generated streak artifacts as in Figure 11(a) by disregarding the projections passing through the pixels occupied by the metal to compute the likelihood. The approach becomes practical if a priori knowledge of the location of rigid metallic tools and their attenuation coefficients in the field of view of the scanner is available using specialized commercial tracking tools (such as those marketed by Polaris).

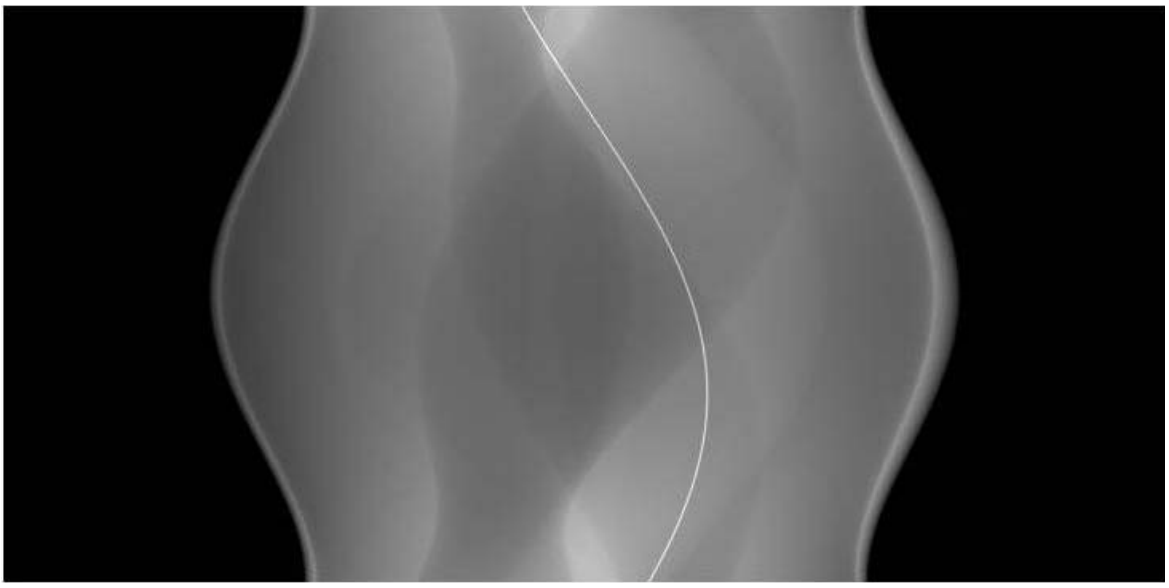

Figure 10: Parallel beam sinogram of the digital phantom of Figure 9 with a high-intensity pixel (number of projections in degrees against number of detectors).

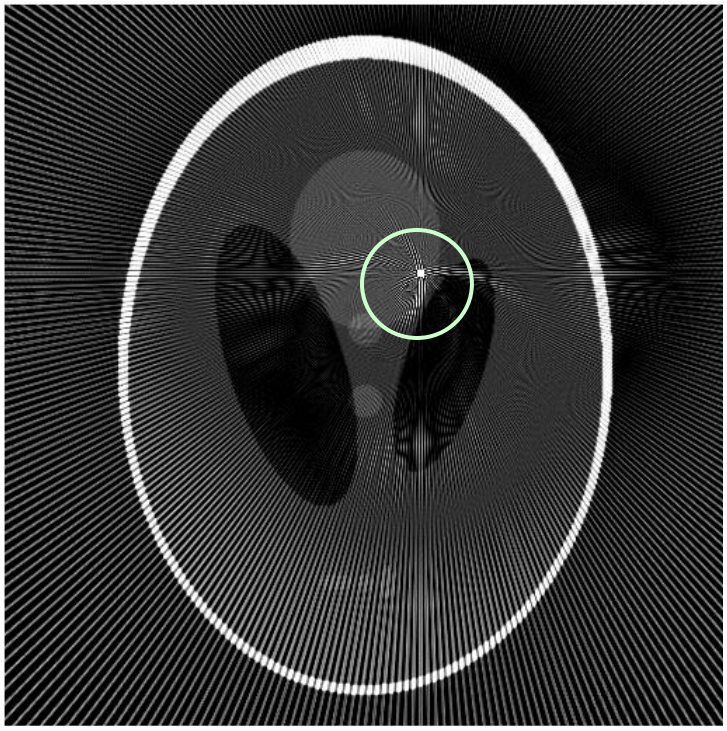

(a) Streak artifacts from the metal after reconstruction using FBP (highlighted for clarity).

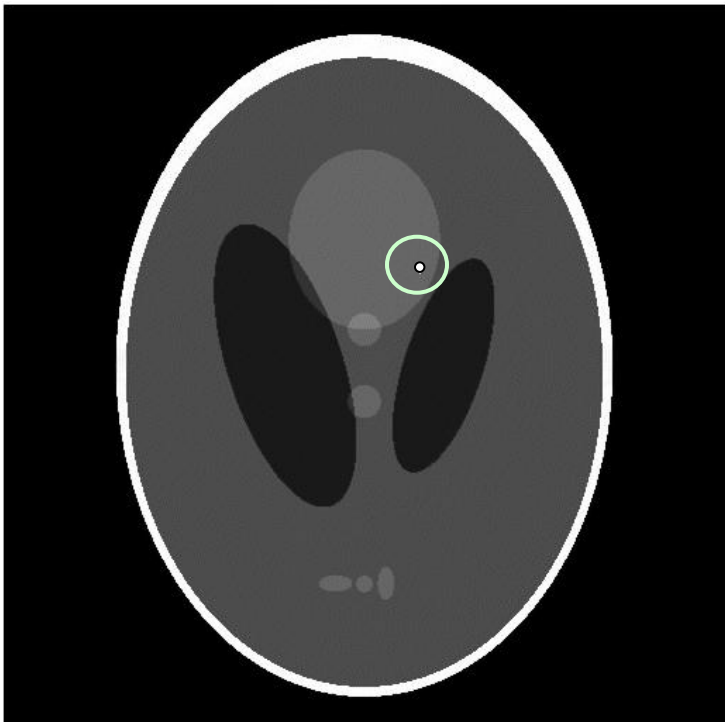

(b) Metal artifact reduction using MLEM and tracking information.
Figure 11: Metal artifact comparison.

4.4. Feasibility of a continuous CT scan (Further dose reduction)

To demonstrate our second strategy of dose reduction, the digital phantom was randomly deformed using the FFD B-spline technique (using Eq. 5 and 6) [12] and projections were generated using the Radon transform. Using the undeformed image as the initial estimate and sum of squared differences between radon transforms as the cost function, the image was iteratively updated through gradient descent optimization method (Eq. 7). For the abdominal phantom, a randomly deformed image of the original phantom was used as the initial estimate and the projection data from the original phantom was used to iteratively converge to the original image using gradient descent optimization.

The number of projections used to compute the cost function was subsequently reduced and convergence was achieved without compromising the image quality in terms of PSNR. It was observed that using only a sixth of the original number of projections (30 instead of 180) does not affect the reconstruction quality for a digital Shepp-Logan phantom.

Figure 12: Original deformed image (left) Recovered deformed image using gradient descent optimization (right) (1st data set).

A visual comparison (Figure 12, Figure 16 and Figure 20) shows that the optimized image matches the original deformed image. The difference images (Figure 13, Figure 17 and Figure 21) provide a better visual assessment of the algorithm. Further, a quantitative assessment of the algorithm was studied through the convergence of the cost function plots of Figure 14, Figure 18 and Figure 22. The PSNR values of Figure 15, Figure 19 and Figure 23 as a function of the number of iterations are monotonously increasing.

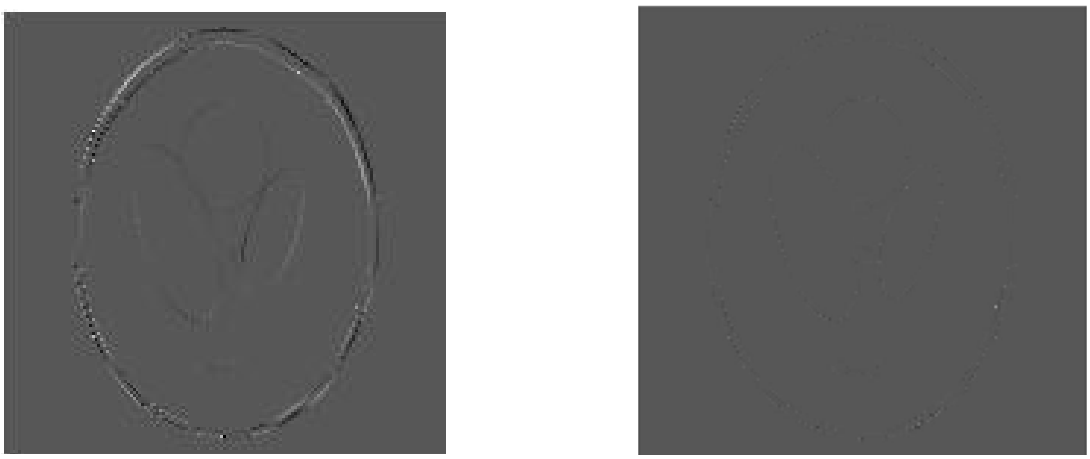

Figure 13: Difference image of the original deformed image and its initial estimate (left), Difference image of the original deformed image and its estimate after convergence (right) (for Figure 12)

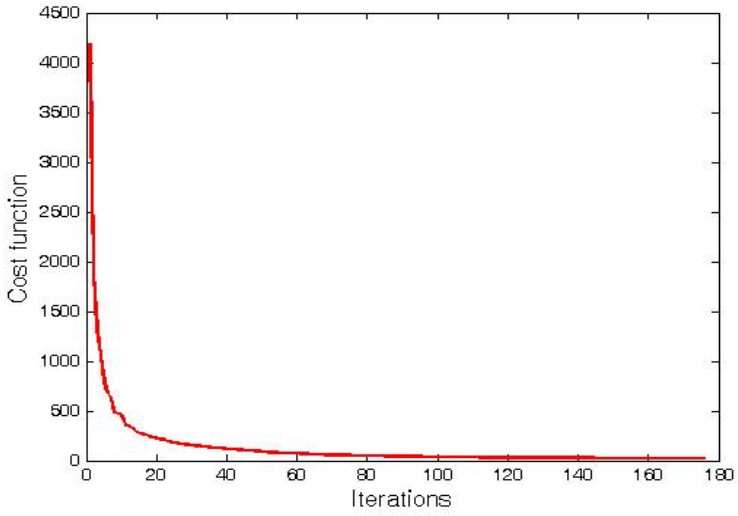

Figure 14: Cost function as a function of the number of iterations for Figure 12. (Note the convergence of the cost function).

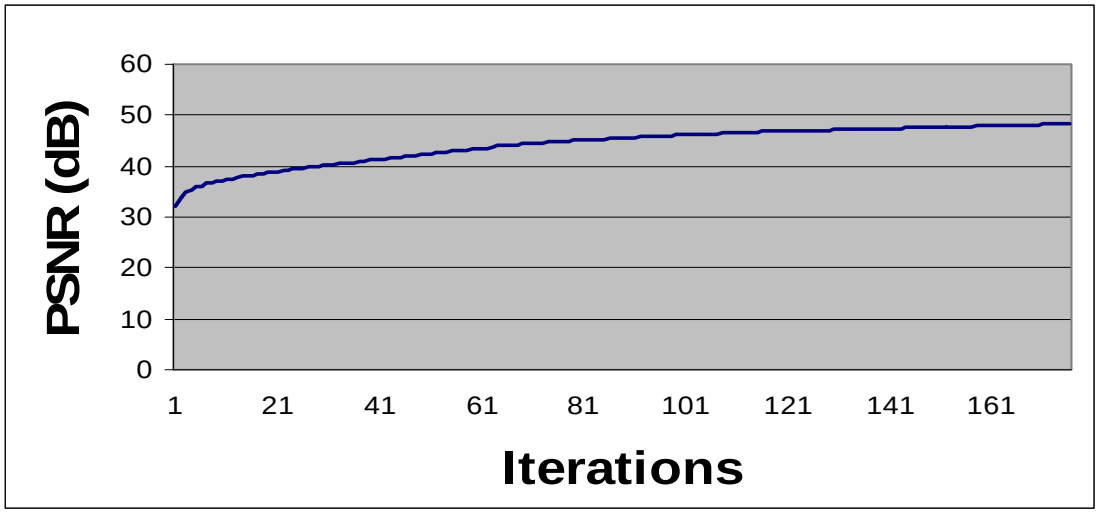

Figure 15: PSNR as a function of number of iterations for Figure 12.
(Note the improvement of image quality in terms of PSNR as the number of iterations increases).

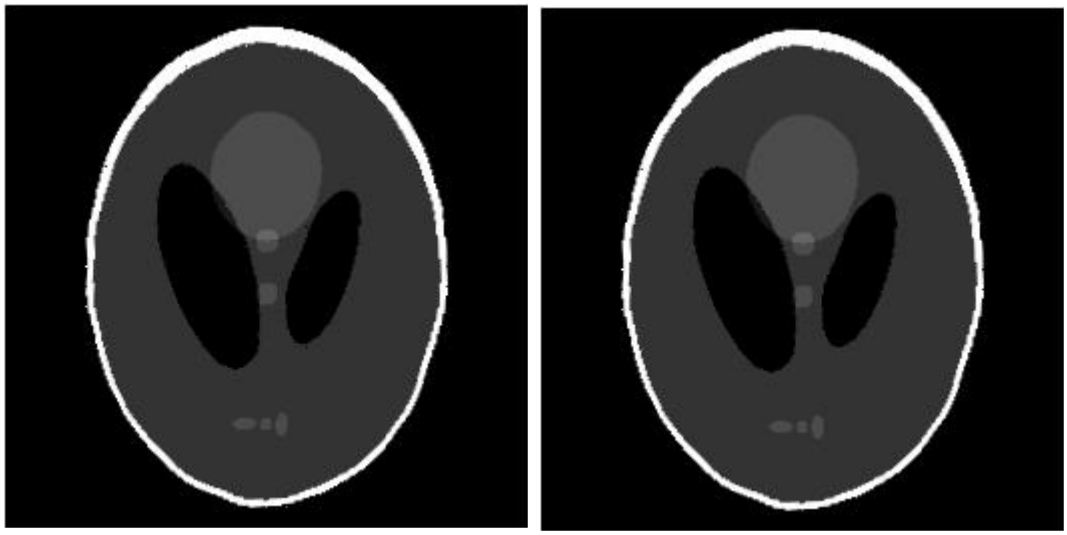

Figure 16: Original deformed image (left) Recovered deformed image using gradient descent optimization (right) (2^{nd} data set).

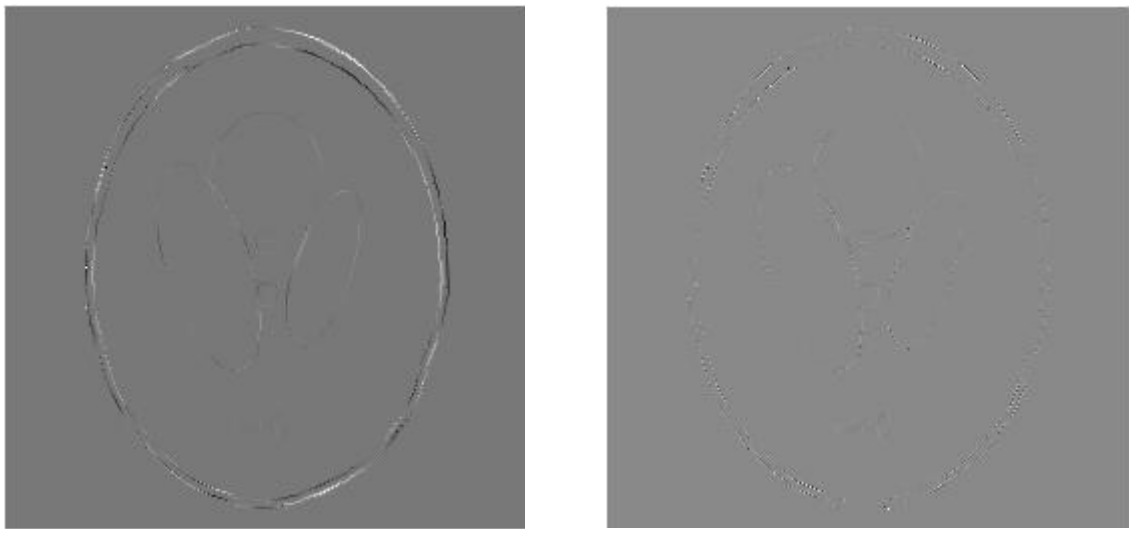

Figure 17: Difference image of the original deformed image and its initial estimate (left), Difference image of the original deformed image and its estimate after convergence (right) (for Figure 16)

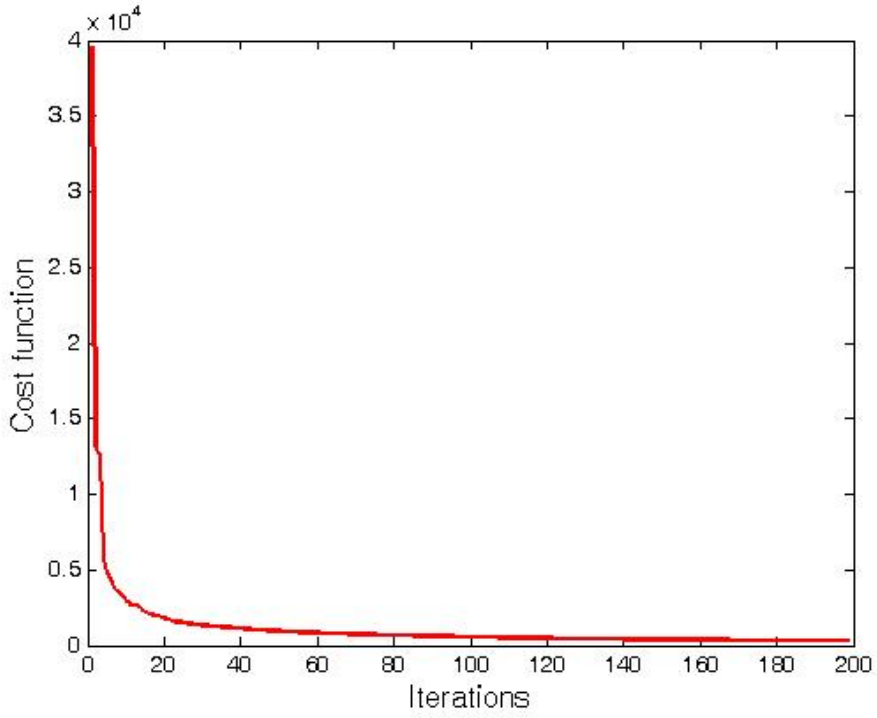

Figure 18: Cost function as a function of the number of iterations for Figure 16. (Note the convergence of the cost function).

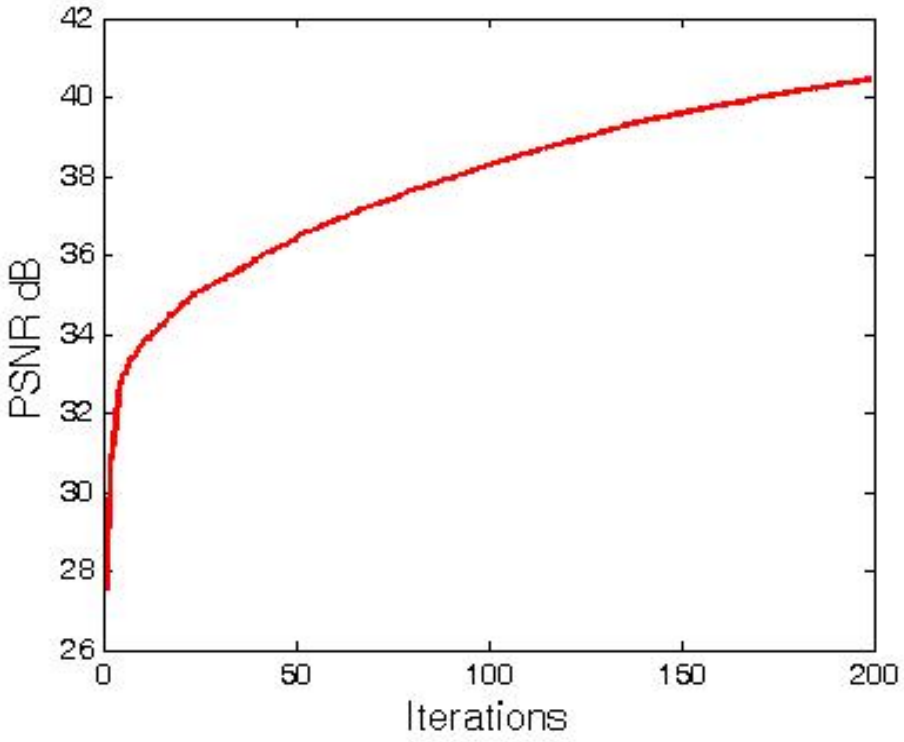

Figure 19: PSNR as a function of number of iterations for Figure 16.
(Note the improvement of image quality in terms of PSNR as the number of iterations increases).

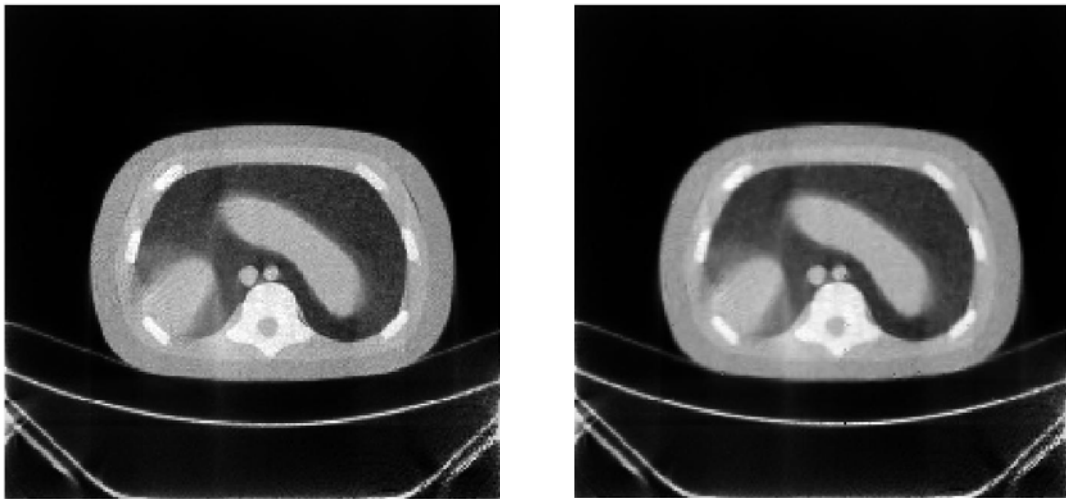

Figure 20: Original deformed image (left) Recovered deformed image using gradient descent optimization (right) (for abdominal phantom).

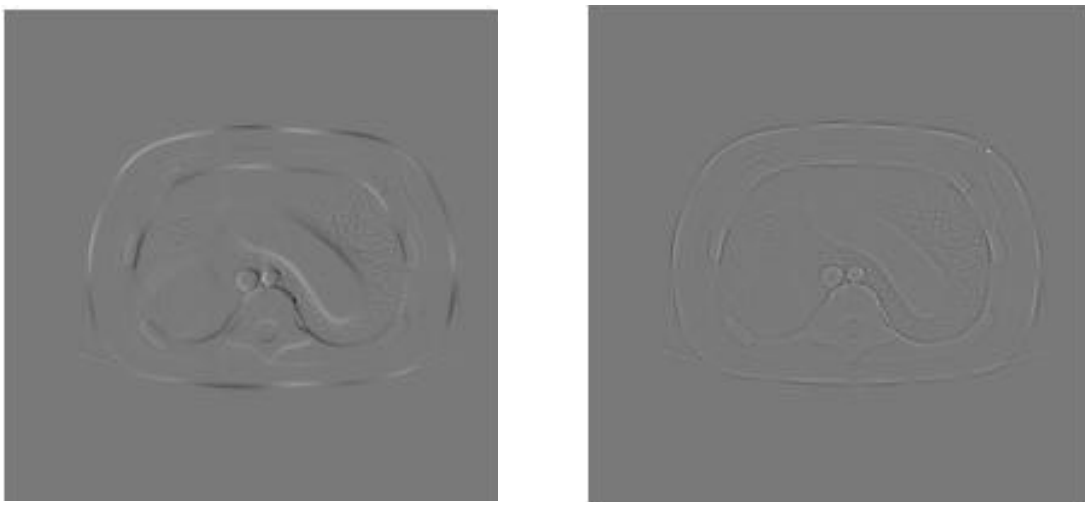

Figure 21: Difference image of the original deformed image and its initial estimate (left), Difference image of the original deformed image and its estimate after convergence (right) (for Figure 20).

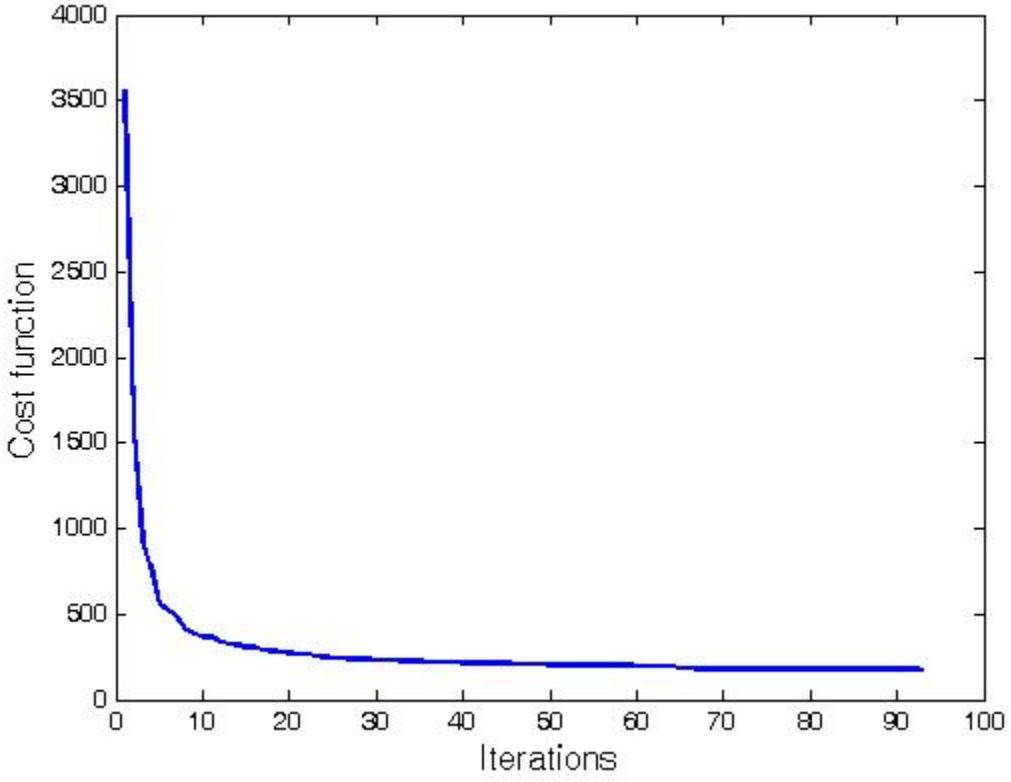

Figure 22: Cost function as a function of the number of iterations for Figure 20.

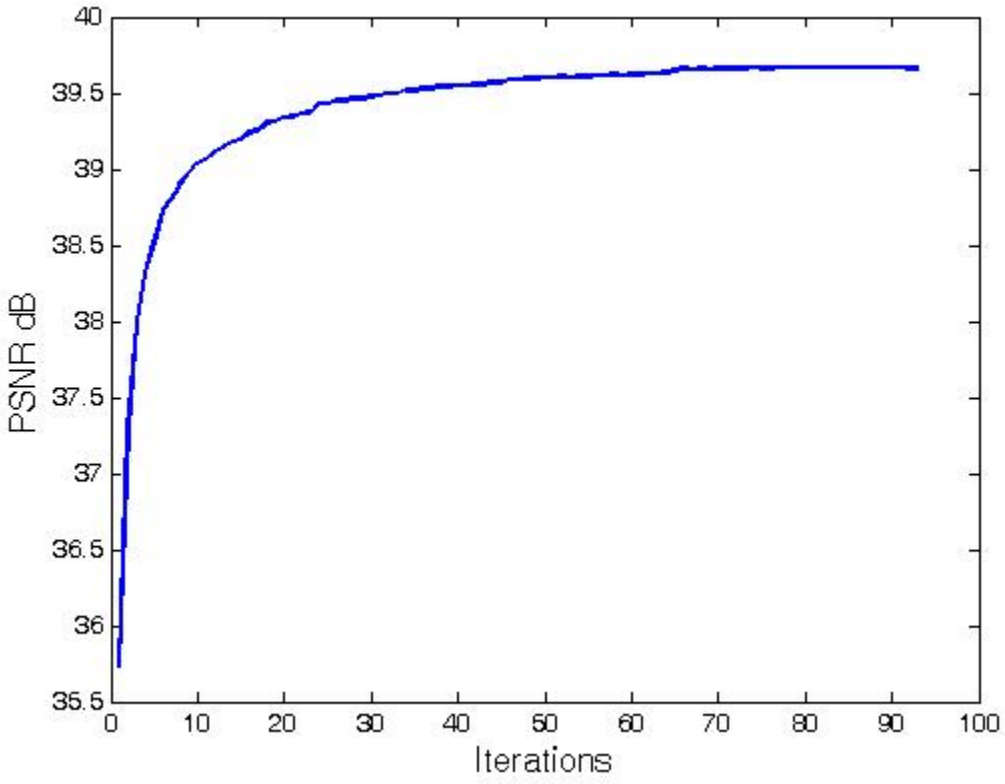

Figure 23: PSNR as a function of number of iterations for Figure 20.

The cost function, for a reduced subset of projections (evenly spaced over 180^{o}), was minimized using gradient descent optimization. The number of projections used for the computation of the cost function was minimized from 180 to 30 for the digital phantom and from 1160 to 29 for the abdominal phantom. Visual assessments of the deformation recovery are provided in Figure 24 and Figure 25. The PSNR comparison (Figure 28) shows that the image quality remains virtually unchanged with the use of partial projections (from 180 down to 30). The quality degrades with further reduction of projections. The cost function (Figure 26 and Figure 27) also converges as the number of iterations increases.

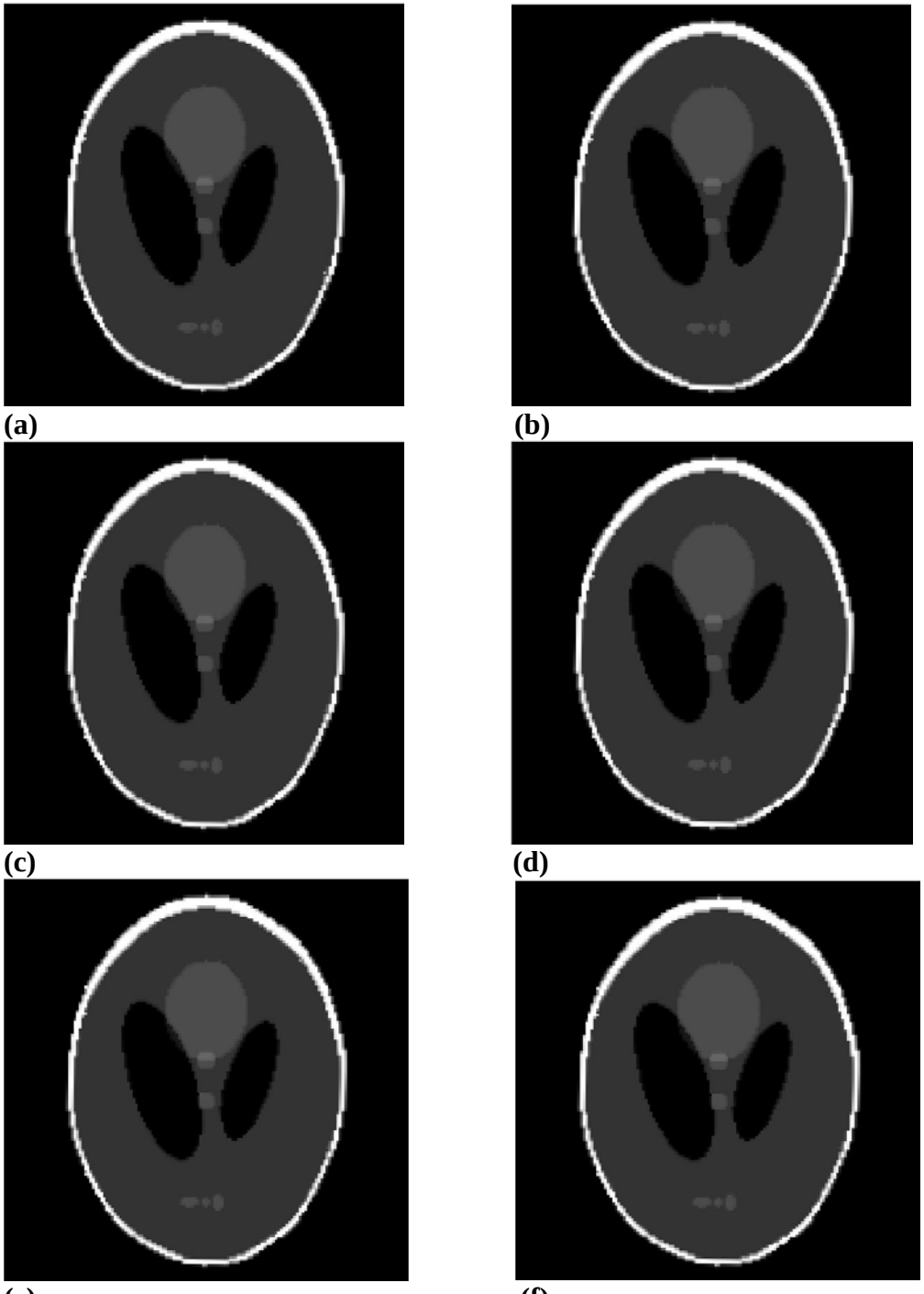

Figure 24: Reduction of dose with fewer projections. Original deformed image (a), Reconstruction using 90 (b), 60 (c), 45 (d), 36 (e), 30 (f) projections.

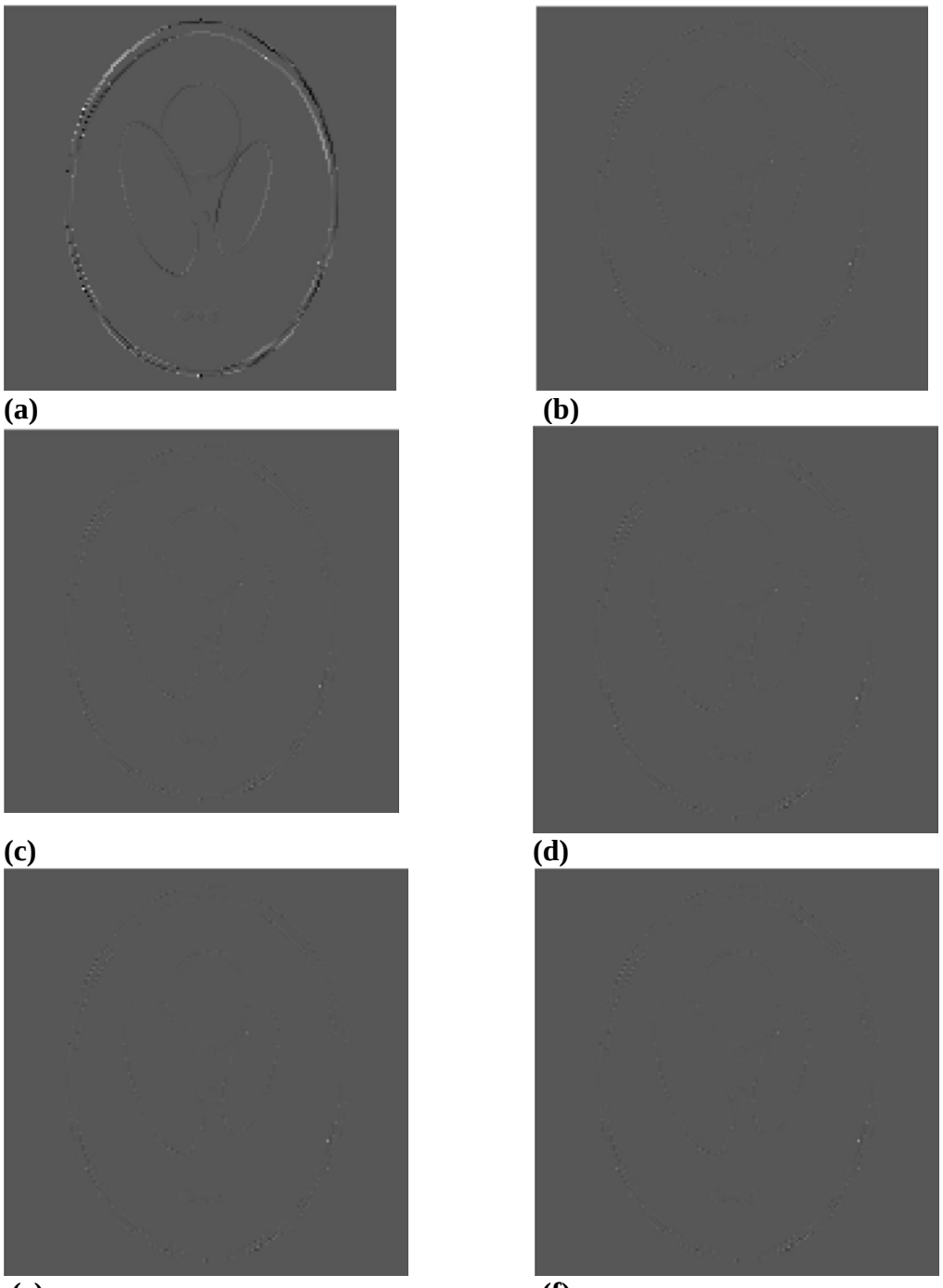

Figure 25: Difference image of the original deformed image with: its initial estimate (a), its estimate after convergence using: 90 (b), 60 (c), 45 (d), 36 (e), 30 (f) projections.

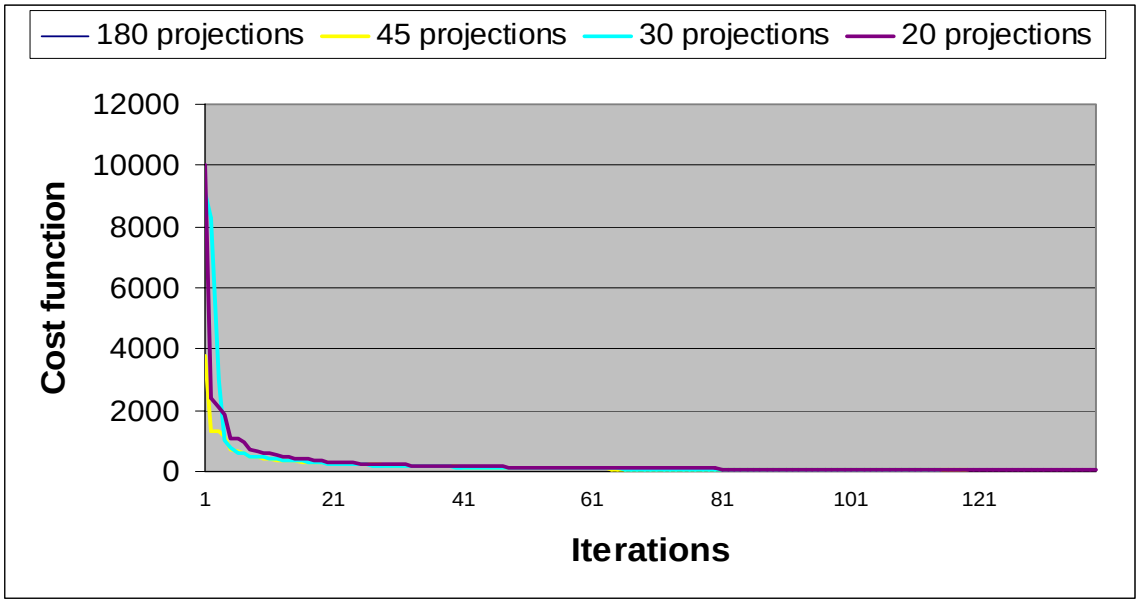

Figure 26: Convergence of the const function using various subsets of projections.

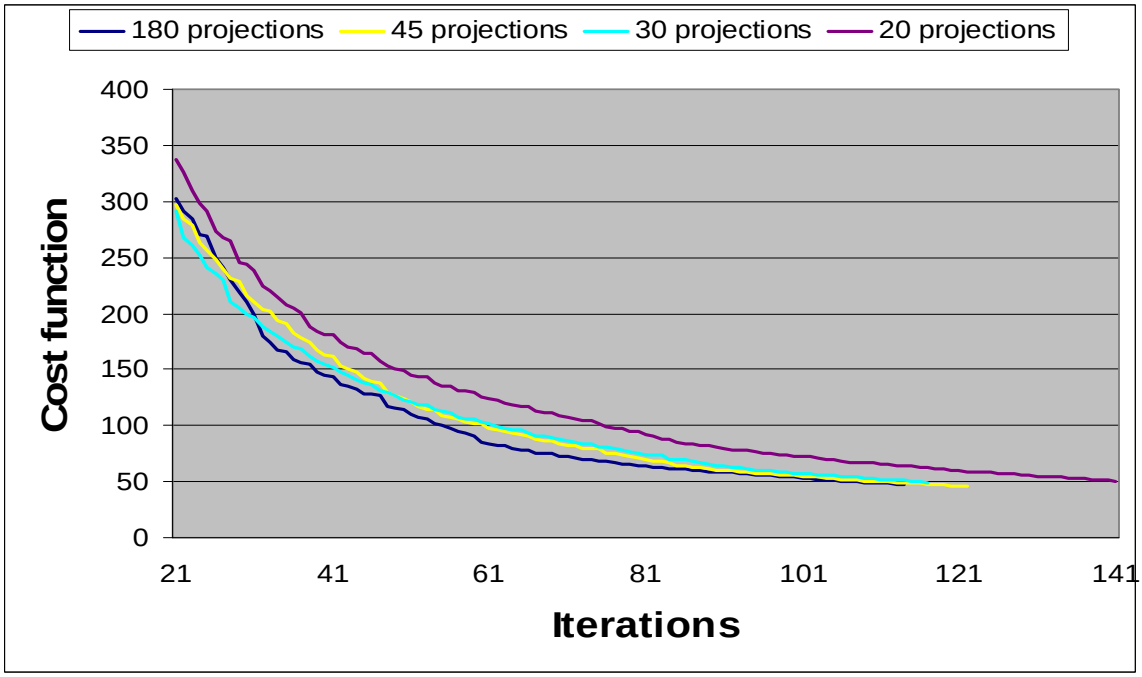

Figure 27: A zoomed-in version of Figure 26 from iteration 20.

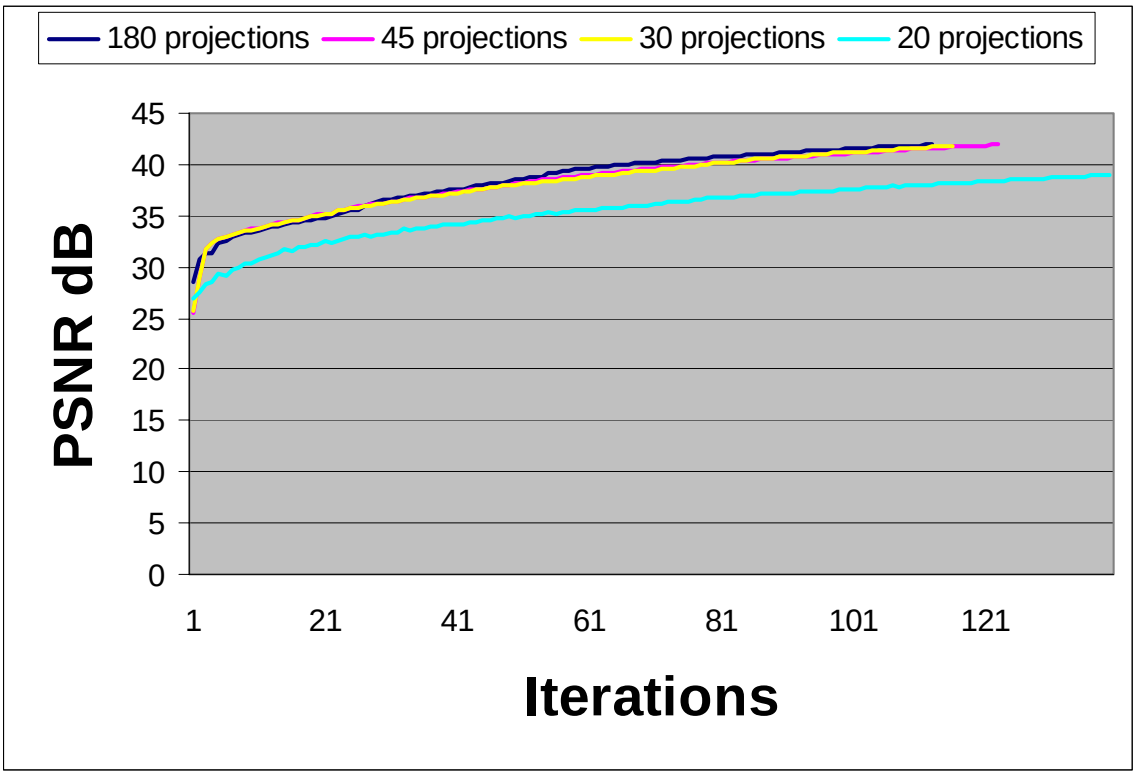

Figure 28: PSNR as a function of the number of iterations for subsets of projections. Image quality is unchanged down to 30 projections.

CHAPTER 5

Discussion

We have demonstrated a reduction in radiation using the MLEM algorithm. The iterative MLEM algorithm incorporates the stochastic properties of x-ray photons while deriving a closed-form solution for attenuation coefficients. The image quality of MLEM was consistently better than that of the corresponding FBP reconstruction for all available doses for a digital phantom. For the abdominal phantom, the image quality degraded much faster for the FBP algorithm than the MLEM algorithm with a reduction in radiation dose. Although PSNR provides a good estimate of image quality for a digital phantom, it is not the best assessment measure for clinical images because of the absence of a standard reference for comparison. However, it shows the general trend of the quality of reconstruction these algorithms provide with respect to the dose value. A comparatively slow deterioration of image quality with decreased dose in the case of the MLEM algorithm could be used to study the feasibility of providing lower dose (tube current) settings on commercial scanners. PSNR does not correlate strongly with the subjective image quality ratings or observer task performance, limiting its utility in image quality assessment investigations [14]. Other assessment measures, such as the just noticeable difference (JND) [15] measure should be investigated in order to provide a more accurate comparison between MLEM and FBP.

The second strategy for dose reduction uses a nonrigid transformation model to describe tissue motion in a continuous CT scan. The algorithm makes no assumption about the physical properties of the tissue. The experimental results have shown that the algorithm

was able to recover the deformed image using the complete set of the projection data. It has been possible to recover the deformed image using only partial subsets of the projection data without considerable change in image quality. Thus a reduction from 180 to 30 projections, which amounts to a dose reduction by a factor of 6 for the digital phantom and a reduction from 1160 to 29 projections, which amounts to a dose reduction by a factor of 40 for the abdominal phantom was achieved. However, values for the initial estimate of the step size and the iterative scaling factor needs to be experimented with to determine their effects on the time for convergence.

The integration of our algorithm in the clinical setting with the use of specialized tracking instruments and markers will successfully eliminate metal artifacts resulting from tools in the field of view. The use of such instruments in a clinical setting was successfully tested in an animal experiment as part of our Operating Room of the Future research. A new technique for dose reduction by modifying the MLEM algorithm is currently under experimentation. It is explained in the next chapter.

Accurate and interactive navigation of image-guided procedures relies on high frame-rate intraoperative imaging and 3D visualization of the involved anatomy, such as that possible with 64-slice CT. Reduced dose will minimize risks associated with prolonged radiation exposure. The achievement of dose reduction, as presented here, establishes the feasibility of an innovative continuous CT-guided visualization and navigation system. This study provides proof-of-concept evidence for dose reduction in two dimensions using an approach that can be extended easily to three dimensions.

CHAPTER 6

6. Scope for further investigation through the extension of MLEM

Modified MLEM algorithm

Our preliminary experiments conducted on the digital Shepp-Logan phantom have proved that the cost function of the MLEM algorithm is optimum when the applied deformation is equal to the actual synthetic deformation.

Keeping the original MLEM framework, two more parameters have been added to limit the deformations between frames.

$$L = \ln(Y, \mu_k(x + \Delta x_k, y + \Delta y_k)$$
$$= \sum_i \sum_j \left\{ \left(M_{ij} - N_{ij}\right) \ln \left(1 - e^{-l_{ij}\mu_j}\right) - N_{ij} l_{ij} \mu_j \right\} + R - \sum_j \left\{ w_1 \left[\left(\Delta \mathrm{x}_j\right)^2 - a \right] + w_2 \left[\left(\Delta \mathrm{y}_j\right)^2 - b \right] \right\},$$

(10)

where R represents terms independent of μ_k and hence independent of the pixel deformations $\Delta \mathrm{x}_k$ and $\Delta \mathrm{y}_k$ in the x- and y-direction.

a and b are the squares of the limiting bounds on the deformations.

In order to compute the maximizing $\Delta \mathrm{x}_k$, derivative of the likelihood is computed to zero

Taking derivative with respect to $\Delta \mathrm{x}_k$

$$\frac{\partial L}{\partial \Delta \mathrm{x}_k} = \frac{\partial L}{\partial \mu_k} \frac{\partial \mu_k}{\partial \Delta \mathrm{x}_k} \tag{11}$$

$$\frac{\partial L}{\partial \Delta x_k} = \sum_i \{\frac{(M_{ik} - N_{ik})}{(1 - e^{-l_{ij}\mu_j})} e^{-l_{ij}\mu_j} l_{ij} - N_{ik} l_{ik}\} \frac{\partial \mu_k}{\partial x} - 2w_1 \Delta x_k$$

$$\frac{1}{e^{l_{ik}\mu_k} - 1} = \frac{1}{l_{ik}\mu_k} - \frac{1}{2} + \frac{l_{ik}\mu_k}{12} + O(l_{ik}\mu_k)^3$$

$$\therefore \frac{\partial L}{\partial \Delta x_k} = -\sum_i \frac{(M_{ik} + N_{ik})}{2} l_{ij} \frac{\partial \mu_k}{\partial x} + \sum_i \frac{(M_{ik} - N_{ik})}{\mu_k + \frac{\partial \mu_k}{\partial x}\Delta x_k + \frac{\partial \mu_k}{\partial y}\Delta y_k} \frac{\partial \mu_k}{\partial x} - 2w_1 \Delta x_k$$

$$\therefore 2w_1 \frac{\partial \mu_k}{\partial x}(\Delta x_k)^2 + \left(2w_1\mu_k + 2w_1 \frac{\partial \mu_k}{\partial y}\Delta y_k + \sum_i \frac{(M_{ik} + N_{ik})}{2} l_{ij} \left(\frac{\partial \mu_k}{\partial x}\right)^2\right)(\Delta x)$$
$$+ \sum_i \frac{(M_{ik} + N_{ik})}{2} l_{ij} \frac{\partial \mu_k}{\partial x}\left(\mu_k + \frac{\partial \mu_k}{\partial y}\Delta y_k\right) - \sum (M_{ik} - N_{ik}) \frac{\partial \mu_k}{\partial x} = 0$$

Simplifying results in 2 solutions given by

$$\Delta x = \left\{ \begin{array}{l} -\left[2w_1\mu_k + 2w_1 \frac{\partial \mu_k}{\partial y}\Delta y_k + \sum \frac{M_{ik} + N_{ik}}{2} l_{ik} \left(\frac{\partial \mu_k}{\partial x}\right)^2\right] \\ \pm \sqrt{\left[2w_1\mu_k + 2w_1 \frac{\partial \mu_k}{\partial y}\Delta y_k + \sum \frac{M_{ik} + N_{ik}}{2} l_{ik} \left(\frac{\partial \mu_k}{\partial x}\right)^2\right]^2 + 8w_1 \left(\frac{\partial \mu_k}{\partial x}\right)^2 \sum_i (Mik - Nij)} \end{array} \right\} \frac{1}{4w1 \frac{\partial \mu_k}{\partial x}}$$

A quadratic equation similar to the one obtained for Δx_k follows for Δy_k

$$2w_2 \frac{\partial \mu_k{}^0}{\partial y}(\Delta y_k)^2 + \left(2w_2\mu_k{}^0 + 2w_2 \frac{\partial \mu_k{}^0}{\partial x}\Delta x_k + \sum_i \frac{M_{ik} + N_{ik}}{2} l_{ik} \left(\frac{\partial \mu_k{}^0}{\partial y}\right)^2\right)(\Delta y_k)$$
$$+ \sum \frac{(M_{ik} + N_{ik})}{2} l_{ik} \frac{\partial \mu_k{}^0}{\partial y}\left(\mu_k{}^0 + \frac{\partial \mu_k{}^0}{\partial x}\Delta x_k\right) - \sum (M_{ik} - N_{ik}) \frac{\partial \mu_k{}^0}{\partial y} = 0$$

$$2w_2\frac{\partial\mu_k{}^0}{\partial y}(\Delta y_k)^2+\left(2w_2\mu_k{}^0+\sum_i\frac{M_{ik}+N_{ik}}{2}l_{ik}\left(\frac{\partial\mu_k{}^0}{\partial y}\right)^2\right)(\Delta y_k)+\sum\frac{(M_{ik}+N_{ik})}{2}l_{ik}\frac{\partial\mu_k{}^0}{\partial y}\mu_k{}^0$$
$$-\sum(M_{ik}-N_{ik})\frac{\partial\mu_k{}^0}{\partial y}+\left(2w_2\frac{\partial\mu_k{}^0}{\partial x}\Delta y_k+\sum\frac{M_{ik}+N_{ik}}{2}l_{ik}\frac{\partial\mu_k{}^0}{\partial x}\frac{\partial\mu_k{}^0}{\partial y}\right)\Delta x_k=0$$

Substituting the value of Δx_k from above in the quadratic equation in Δy_k

yields

$$\therefore\ \sum\frac{(M_{ik}+N_{ik})}{2}l_{ik}\frac{\partial\mu_k{}^0}{\partial y}\mu_k{}^0-\sum(M_{ik}-N_{ik})\frac{\partial\mu_k{}^0}{\partial y}+\frac{1}{4w_1}\left(2w_2\Delta y_k+\sum\frac{M_{ik}+N_{ik}}{2}l_{ik}\frac{\partial\mu_k{}^0}{\partial y}\right)$$
$$\text{x}\left\{\begin{array}{l}-\left[2w_1\mu_k{}^0+2w_1\dfrac{\partial\mu_k{}^0}{\partial y}\Delta y_k+\sum\dfrac{M_{ik}+N_{ik}}{2}l_{ik}\left(\dfrac{\partial\mu_k{}^0}{\partial x}\right)^2\right]\\ \pm\left\{\left(2w_1\dfrac{\partial\mu_k{}^0}{\partial y}\Delta y_k+2w_1\mu_k{}^o-\sum\dfrac{M_{ik}+N_{ik}}{2}l_{ik}\left(\dfrac{\partial\mu_k{}^0}{\partial x}\right)^2\right)^2+8w_1\left(\dfrac{\partial\mu_k{}^0}{\partial x}\right)^2\sum(M_{ik}-N_{ik})\right\}^{1/2}\end{array}\right\}$$
$$+2w_2\frac{\partial\mu_k{}^0}{\partial y}(\Delta y_k)^2+\left(2w_2\mu_k{}^0+\sum_i\frac{M_{ik}+N_{ik}}{2}l_{ik}\left(\frac{\partial\mu_k{}^0}{\partial y}\right)^2\right)(\Delta y_k)=0$$

Solving for Δy_k and Δx_k yields two solutions given by

$$\Delta y_k=\frac{-\partial\mu_k/\partial y}{4w_2D}\left\{-(2w_1w_2\mu_k+(avg)D)\pm\sqrt{(2w_1w_2-(avg)D)^2+8w_1w_2(abs)D}\right\} \tag{12}$$

$$\Delta x_k=\frac{-\partial\mu_k/\partial x}{4w_1D}\left\{-(2w_1w_2\mu_k+(avg)D)\pm\sqrt{(2w_1w_2-(avg)D)^2+8w_1w_2(abs)D}\right\} \tag{13}$$

$$avg=\sum\frac{M_{ik}+N_{ik}}{2}l_{ik},\quad abs=\sum(M_{ik}-N_{ik}),\quad D=w_1\left(\frac{\partial\mu_k}{\partial y}\right)^2+w_2\left(\frac{\partial\mu_k}{\partial x}\right)^2$$

It is hypothesized that an appropriate selection of w_1 and w_2 will provide a maximizing value for Δx_k and Δy_k.

Thus a closed-form solution can be found for the intraoperative anatomic deformations for a coarse grid of pixels overlaid on the image. A B-spline interpolation, then, over the entire image would yield a smooth deformed image. We propose that a successful implementation of the modified MLEM algorithm would result in a dose reduction through the reduction in number of projections for our continuous CT application, a feasibility of which can only be determined through experimentation.

References

[1] Cleaveland Clinic Foundation, “Minimally Invasive Cardiovascular and Thoracic Surgeries”, 20 Nov. 2006, <http://www.clevelandclinic.org/heartcenter/pub/guide/disease/mini_invasivehs.htm>

[2] A. S. Shetye and R. Shekhar, "A statistical approach to high quality CT reconstruction at low radiation doses for real-time guidance and navigation," *Proc. SPIE Med. Imaging*, [In Press].

[3] J. Browne and A. R. De Pierro, "A row-action alternative to the EM algorithm for maximizing likelihoods in emission tomography," *IEEE Trans. Med. Imaging*, vol. 15, pp. 687-699, 1996.

[4] B. De Man, J. Nuyts, P. Dupont, G. Marchal, and P. Suetens, "An iterative maximum-likelihood polychromatic algorithm for CT," *IEEE Trans. Med. Imaging*, vol. 20, pp. 999-1008, 2001.

[5] I. A. Elbakri and J. A. Fessler, "Statistical image reconstruction for polyenergetic x-ray computed tomography," *IEEE Trans. Med. Imaging*, vol. 21, pp. 89-99, 2002.

[6] J. A. Fessler and A. O. Hero, "Penalized maximum-likelihood image reconstruction using space-alternating generalized EM algorithms," *IEEE Trans. Image Proces.*, vol. 4, pp. 1417-1429, 1995.

[7] K. Lange and R. Carson, "EM reconstruction algorithms for emission and transmission tomography," *Jour. Comput. Assist. Tomogr.*, vol. 8, pp. 306-316, 1984.

[8] L. A. Shepp and Y. Vardi, "Maximum likelihood reconstruction for emission tomography," *IEEE Trans. Med. Imaging*, vol. 1, pp. 113-122, 1982.

[9] American Physical Society, “CT scans”, 11 Dec. 2006, <http://www.physicscentral.com/action/2002/scans.html>.

[10] W. A. Kalender, “Review x-ray computed tomography,” *Phys. Med. Biol.,* vol. 51, pp. R29-R43, 2006.

[11] A. C. Kak and M. Slaney, *Principles of computerized tomographic imaging*. New York: IEEE press, NY, 1988.

[12] D. Rueckert, L. I. Sonoda, C. Hayes, D. L. G. Hill, M. O. Leach, and D. J. Hawkes, "Nonrigid registration using free-form deformations: application to breast MR images," *IEEE Trans. Med. Imaging*, vol. 18, pp. 712-721, 1999.

[13] P. A. Rattey and A. G. Lindgren, "Sampling the 2-D Radon Transform," *IEEE Trans. Acoust., Speech, Signal Proces.*, vol. 29, pp. 994-1002, 1981.

[14] W. F. Good, D. Gur, J. H. Feist, F. L. Thaete, C. R. Fuhrman, C. A. Britton and B. S. Slasky, "Subjective and objective assessment of image quality- a comparison," *Jour. Digital Imaging*, 7(2), pp. 77-8, 1994.

[15] K. M. Siddiqui, J. P. Johnson, B. I. Reiner, E. L. Siegel, "Discrete cosine transform JPEG compression vs. 2D JPEG2000 compression: JNDmetrix visual discrimination model image quality analysis," *Proc. SPIE,* vol. 5748, pp. 202-207, 2005.

[16] P. J. La Rivière and D. Billmire, "Reduction of noise-induced streak artifacts in x-ray computed tomography through spline-based penalized-likelihood sinogram smoothing," *IEEE Trans. Med. Imaging*, vol. 24, pp. 105-111, 2005.

[17] P. J. La Rivière and X. Pan, "Nonparametric regression sinogram smoothing using a roughness-penalized poission likelihood objective function," *IEEE Trans. Med. Imaging*, vol. 19, pp. 773-786, 2000.

[18] T. Lei and W. Sewchand, "Statistical approach to x-ray CT imaging and its application in image analysis," *IEEE Trans. Med. Imaging*, pp. 53-61, 1992.

[19] T. Li, X. Li, J. Wang, J. Wen, H. Lu, J. Hsieh, and Z. Liang, "Nonlinear sinogram smoothing for low-dose x-ray CT," *IEEE Trans. Nuc. Sci.*, vol. 51, pp. 2505-2513, 2004.

[20] A. Papoulis, *Random variables and stochastic processes*. New York: McGraw Hill Book company, NY, 1965.

[21] G. Wang, T. Frei, and M. W. Vannier, "Fast iterative algorithm for metal artifact reduction in x-ray CT," *Acad. Radiol.*, vol. 7, pp. 607-614, 2000.

[22] J. Wang, T. Li, H. Lu, and Z. Liang, "Penalized weighted least-squares approach to sinogram noise reduction and image reconstruction for low-dose x-ray computed tomography," *IEEE Trans. Med. Imaging*, vol. 25, pp. 1272-1283, 2006.

[23] Z. Wei, G. Li, and L. Qi, "New nonlinear conjugate gradient formulas for large-scale unconstrained optimization problems," *Appl. Math. Comput.*, vol. 179, pp. 407-430, 2006.

[24] B. R. Whiting, "Signal statistics of x-ray CT," *Proc. SPIE Med. Imaging*, vol. 4682, pp. 53-60, 2002.

[25] A. Ziegler, T. Nielsen, and M. Grass, "Iterative reconstruction of a region of interest for transmission tomography," *Proc. SPIE Med. Imaging*, vol. 6142, pp. 614223, 2006.

[26] G. T. Herman, *Image reconstruction from projections:* Springer-Verlag Berlin Heidelberg, New York, NY, 1979.

[27] M. C. Joshi and K. M. Moudgalya, *Optimization theory and practice*: Alpha Science International Ltd. UK, 1979.

[28] A. d'Aische, M. De Craene, X. Gregoire, B. Macq, and S. K. Warfield, "Efficient multi-modal dense field non-rigid registration: Alignment of histological and section images," *Med. Imaging Anal.,* [In Press].

Avanti Shetye

Email: avshetye@gmail.com Phone: 240-515-8469

Education

- University of Maryland, College Park, MD (Aug 2004-Feb 2007)
  M.S., Electrical & Computer Engineering
- University of Mumbai, India (Aug 2000-May 2004)
  B.E. (Hons.) Electrical & Electronics Engineering; Ranked 11/3000 in the University.

Research Experience

Graduate Research Assistant (Jul 2005-Feb 2007)

Imaging Technologies Laboratory, Diagnostic Imaging, University of Maryland Medical System (UMMS)

Developing a statistical algorithm for computed tomography (CT) reconstruction using low radiation doses for continuous scanning and navigation. The motivation behind this research is to utilize the benefit of 3D visualization achieved through CT for interventional purposes, but at an innocuous radiation dose and without compromising image quality. [MATLAB, C/C++]

Researcher (Jan 2005- Jun 2005)

Speech Communications Laboratory, University of Maryland, College Park

Independently researched analyzing "creakiness" in speech, one voice quality that can be used for speaker recognition, and submitted a 20 page report [MATLAB, Emacs, Xwin32]

Publications

- Avanti Shetye, Raj Shekhar, "***A statistical approach to high-quality CT reconstruction at low radiation doses for real-time guidance and navigation***", Medical Imaging: Image Processing, Proc. SPIE, 2007, accepted for publication
- Avanti S. Shetye & Carol y. Espy-Wilson, "***Analysis of model and creaky voice quality variations***", Journal of the Acoustical Society of America, vol. 118, pp. 1965, 2005

Projects

Medical Imaging [In MATLAB] (Fall 2005)

- Designed & implemented iterative & non-iterative algorithms for reconstruction of PET, SPECT, CT
- Implemented Segmentation algorithm for Ultrasound images
- Implemented rigid registration algorithm for MRI, CT

Avanti Shetye

Email: avshetye@gmail.com Phone: 240-515-8469

Image & Video Compression [In MATLAB] (Spring 2005)

- Implemented JPEG & JPEG2000 compression schemes using DCT, EZW and EBCOT in sequential, hierarchical, lossless & progressive modes
- Extended JPEG to MPEG2 video compression with SNR, spatial & temporal scalability

Multimedia Signal Processing (Fall 2004)

- Addressed fundamental multimedia issues on audio processing, speech recognition & synthesis, and image & video processing using state-of-the-art technologies [MATLAB, C++, IBM via voice].
- Developed an application for making Mapquest interactive and user-friendly while driving with voice recognition and text-to-speech conversion [MS Speech SDK, C++]

Undergraduate level projects

- Designed and programmed a speech recognition & robotic application system aimed at assisting the physically challenged with operation of routine devices using speech [C] (Spring 2004)
- Designed a wireless transmitter using analog and digital devices with a potential to transmit over 250 meters (Fall 2003)

Relevant Coursework

- Information theory & coding
- Multimedia Signal Processing
- Medical Imaging & Imaging Analysis
- Probability & Stochastic Processes in Communications & Control
- Detection & Estimation theory
- Digital Image Processing
- Advanced DSP & adaptive filter design
- Modeling, Analysis, & optimization of Embedded Software

Academic Achievements

- Sir Ratan Tata Trust Scholarship for academic excellence in sophomore and junior years of BE (2002-03)
- JRD Tata Trust Scholarship in the junior year of BE (2003)
- National Talent Scholarship (N.T.S.) by the National Council of Educational Research and Training (Was in the top 750 out of more than a million students all over India) (1998)
- Third position at the city level and twenty-second position at the State level (among more than 10,000 students) in academic Talent Search examinations (1996-1998)

Avanti Shetye

Email: avshetye@gmail.com Phone: 240-515-8469

Skills

- Software languages – MATLAB, Pascal, C, C++, PHP
- Assembly languages – 8085, 8086, 80286, 80386, 8051, Pentium
- Operating system – MS DOS, WINDOWS 95/98/2000/NT/XP, UNIX
- Applications – MS Office Suite, Microsoft Visio, X-windows, Emacs, Adobe Photoshop, HTML, Dreamweaver, SQL, Crystal Reports, Praat

Other Professional Activities

- Student Member – IEEE (The institute of Electrical and Electronics Engineers, Inc.) (2005-2007)
- Student Head of Electrical Engineering Department during the Technical Festival Technovanza of the senior year of BE (2003-04)
- General Secretary, Electrical Engineers' Student Association (EESA) - organized technical activities (2001-02)
- EESA Librarian - Conceived & created the EESA library for Electrical Engineers (2001-02)

Languages – English (Fluent), French (Written language), Hindi (Fluent)